Electronic Supplementary Information

Repulsive anode interface for high-energy and safe lithium metal batteries

Jihoon Oh,[a,b] Joseph L. Frank,[c] Randolph A. Leising,[c] Heejin Kim,[d] Jisub Kim,[a,b] Minkwan Kim,[a,b] and Jang Wook Choi*[a,b]

[a.] *School of Chemical and Biological Engineering and Institute of Chemical Process, Seoul National University, Seoul, Republic of Korea. E-mail: jangwookchoi@snu.ac.kr*
[b.] *Hyundai Motor Group-Seoul National University (HMG-SNU) Joint Battery Research Center (JBRC), Seoul National University, Seoul, Republic of Korea*
[c.] *SES AI Corporation, Woburn, MA, USA*
[d.] *Division of Analytical Science, Korea Basic Science Institute, Daejeon, Republic of Korea*
† Electronic Supplementary Information (ESI) available: See DOI: 10.1039/x0xx00000

Experimental Section

Computational methods. DFT calculations were performed using the Vienna ab-initio simulation package (VASP)[1] with the Perdew-Burke-Ernzerhof (PBE) exchange-correlation functional.[2] The energy cutoff was 520 eV, and the number of k-points per reciprocal atom (KPPRA) was 1200. Convergence criteria were 10^{-7} eV and 0.01 eV $Å^{-1}$ for electronic and ionic steps, respectively. Mixing configurations between the transition metal and Li atoms were generated using Alloy Theoretic Automated Toolkit (ATAT) software.[3,4] Additionally, mixing configurations with low heteroatom content (e.g., 0.78 at% Li in the W host) that were not explored by ATAT were considered manually. The configurational entropy term ($-kT(x\ln_x A + xB\ln_x B)$) was added to the calculated enthalpy to estimate the free energy. The obtained effective cluster interaction (ECI) values were utilized to conduct Monte Carlo simulations and predict the phase boundary, as implemented in ATAT. Computational details for modeling the interface between Li metal and the target materials (W, Ti, Ag, and LiF) are presented in Note S1–4, ESI†.

Separator and electrode preparation. The W-PE separator was fabricated by a PVD metal sputtering process. To ensure structural integrity during deposition, the PE membrane was affixed to a stainless-steel (SUS) substrate. Sputtering was carried out under optimized conditions: DC power: 300 W; sputtering gas: high-purity argon (Ar); process pressure: 2 mTorr; target-substrate distance: 15 cm. W coatings were applied to both sides of the PE in Li-Li symmetric and Li-Cu asymmetric cells, whereas sequential boehmite and W coatings were employed for the W-PE used in full-cells. The thickness of the W protective layer was precisely maintained at 30 nm and the uncoated PE served as the control. Cathodes for full-cell evaluations were prepared using a slurry casting method. The NCM811 cathode active material was combined with SuperP and PVDF binder in a 96:2:2 weight ratio and then dispersed in NMP solvent to create a uniform slurry. This slurry was applied to Al foil using the doctor blade technique. The coated cathodes were dried in a vacuum oven at 60 °C for 12 hours to eliminate residual solvent. The final cathode mass loading was 15 mg cm^{-2} for coin cell-based evaluations.

Characterization techniques. The depth profiling of W-PE was performed using a ToF-SIMS 5 instrument (ION-ToF GmbH, Germany). Surface and cross-sectional images were captured using field emission scanning electron microscopy (FE-SEM, JSM-7800F Prime, JEOL). 3D visualization was accomplished using an integrated high-resolution X-ray microscopy and computed tomography system (Xradia 620 Versa, Carl Zeiss) at Seoul National University's National Center for Inter-University Research Facilities (NCIRF). For this analysis, the Li metal and separators were exposed to X-rays for 6 hours using the following settings: 80 kV voltage, 125 μA current, and 10 W power. Image resolution was set to 0.5 pixels per unit. The resulting data were processed to reconstruct both 3D and 2D structures using imaging software (Dragonfly 2021.1, Object Research Systems).

Electrochemical analysis. Electrochemical measurements were conducted using CR2032 coin cells assembled in an argon-filled glovebox or pouch-cells in a dry-room environment. Each coin cell contained 60 μL of electrolyte, consisting of 1 M $LiPF_6$ in EC/DEC (50/50 = v/v) with 10 wt% FEC. Galvanostatic charge-discharge cycles were recorded using a battery cycler (WBCS3000, WonATech, South Korea). EIS measurements were performed using a potentiostat (VSP, Bio-Logic, France) over a frequency range of 1 mHz to 1 MHz. Full-cell tests utilized the aforementioned NCM811 cathodes, and all coin cell-based full-cells underwent activation with three formation cycles at 0.1C (1C=200 mA g^{-1}) within a 3.0−4.3 V voltage range, at constant temperature of 25 °C.

Pouch-cell fabrication. Pouch-cell assembly was meticulously performed in a dry room maintained at a dew point below −55 °C. 30 × 40 mm^2 pouch-cells were constructed as follows: electrodes (Li metal anode and NCM811 cathode) and separators were precisely cut using a punching machine, then systematically stacked and sealed in a laminate bag. The W-coated side of the separator was placed facing the Li metal anode, while the boehmite-coated side faced the cathode. A lean electrolyte was added before vacuum-sealing the bag. The electrolyte composition (1 M $LiPF_6$ in EC/DEC (50/50 = v/v) with 10 wt% FEC) was identical to that used in coin-cell evaluations, except for the pouch-cells fabricated by SES AI Corp., which employed 2 M LiFSI in TFDMP.[5]

Note S1 Calculation of interface between Li and W.

Since bcc metals share the same crystal symmetry as Li metal, we assumed a coherent interface between Li metal and W.[6] In the calculations, we used 4–6 W layers and systematically increased the number of Li layers. To validate this computational model, we tested larger models with 10 W layers (approximately 20 Å thick), and the results were almost identical, with only a 1.9% difference. The in-plane lattice parameters (*a*- and *b*- constants) were fixed to those of the W, while the lattice was allowed to relax in the direction normal to the interface (*c*-direction), to allow the Li metal layer some freedom to grow in this direction. We also tested cases where the lattice parameters were fixed in all directions, and the energy differences were less than 5%. Low-index facets, such as (100), (110), and (111), were examined.

Note S2 Calculation of interface between Li and Ti.

We assumed that Li metal adopts a bcc structure when in contact with hcp Ti. The Ti(100)|Li(100), Ti(110)|Li(100), and Ti(001)|Li(100) interfaces were evaluated. Only the (100) facet of Li metal was considered for the interface, as the effect of the initial Li configuration on the interface energy is known to be minimal in the linear extrapolation scheme.[7] We created rectangular supercells of Ti (~10 × 10 Å in size) such that the lattice mismatch in the planar (*a*- and *b*-) directions was minimized when aligning with the Li metal supercells. The *a*- and *b*- parameters of the Li layer were then adjusted to match the Ti lattice. The initial position of the Li layer in the *a*- and *b*- directions was systematically tested at 4 × 4 grid positions, and the most stable configuration was selected. Similar to the bcc metal (W), the *a*- and *b*- lattice constants were fixed to those of Ti, and the lattice was relaxed only in the direction normal to the interface (c-direction).

Note S3 Calculation of interface between Li and Ag.

Low-index crystallographic facet (100) of fcc Ag was constructed and extended to rectangular supercells (10−14 Å in *a*- and *b*-directions) to minimize in-plane lattice mismatch with bcc Li supercells. The computational models comprised 7 atomic layers of Ag interfaced with 7−13 atomic layers of Li on both surfaces. To identify the most energetically favorable contact configuration, the relative *x*- and *y*-positions of Li layers were systematically sampled at ~1 Å intervals with respect to the underlying Ag substrate. In-plane lattice parameters (*a*, *b*) were constrained to match Ag dimensions, while *c*-axis relaxation remained unconstrained.

Note S4 Calculation of interface between Li and LiF.

As in the case of the hcp metal (Ti), we considered the interface between the low-index facets of the ionic compounds and the (100) facet of the bcc Li metal. For the low-index facets of the ionic compound (LiF), we prepared all possible stoichiometric cutting planes of the (100), (110), and (111) facets. Then, the most stable slab models for each facet were evaluated to construct the interface with the Li metal. The remaining calculation procedures were identical to those ones used for the hcp metal (Ti).

Table. S1 Binary phase information of the Li–W system.

Phase	Composition (% W)	Space group
βLi	0	$Im\bar{3}m$
αLi	0	$P6_3/mmc$
W	100	$Im\bar{3}m$

Note: The Li–W system exhibits no intermediate phases; only pure Li and pure W (0% or 100% W) have been reported to date.[8]

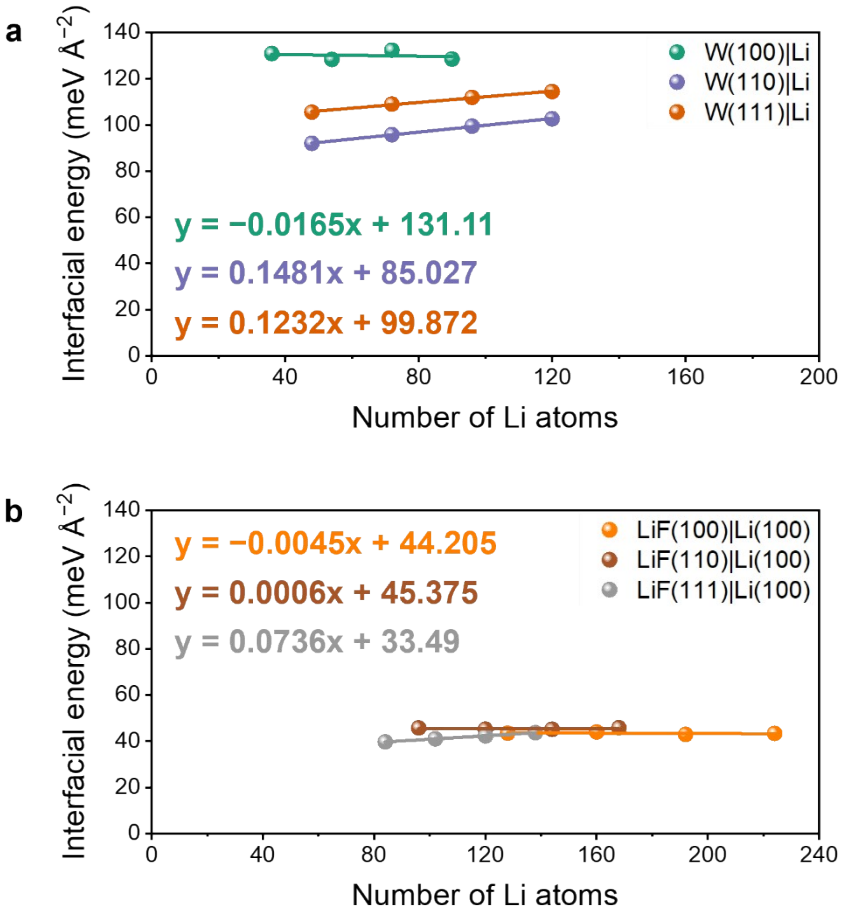

Fig. S1 DFT-calculated Li interfacial energies of (a) W metal and (b) LiF.

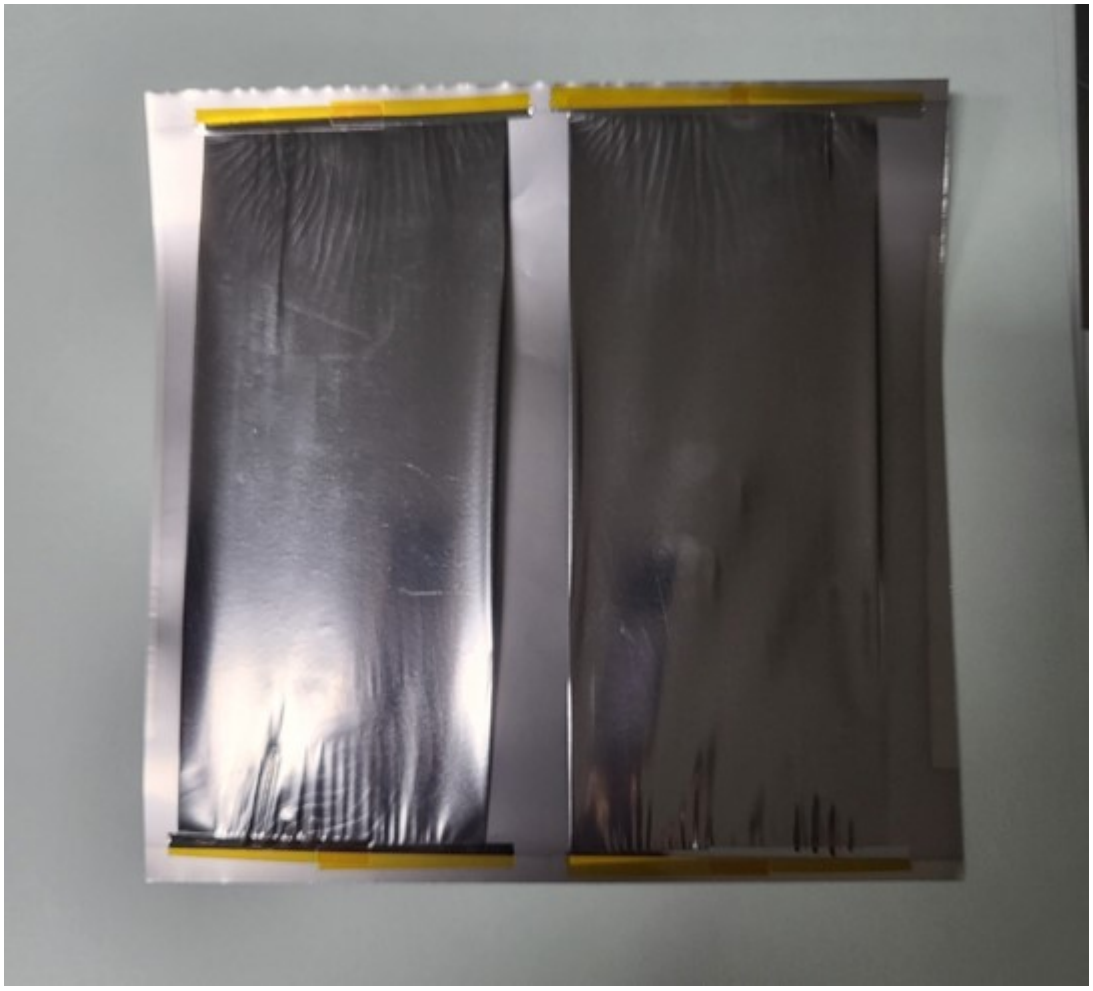

Fig. S2 Digital photograph of the W-PE after the sputtering process.

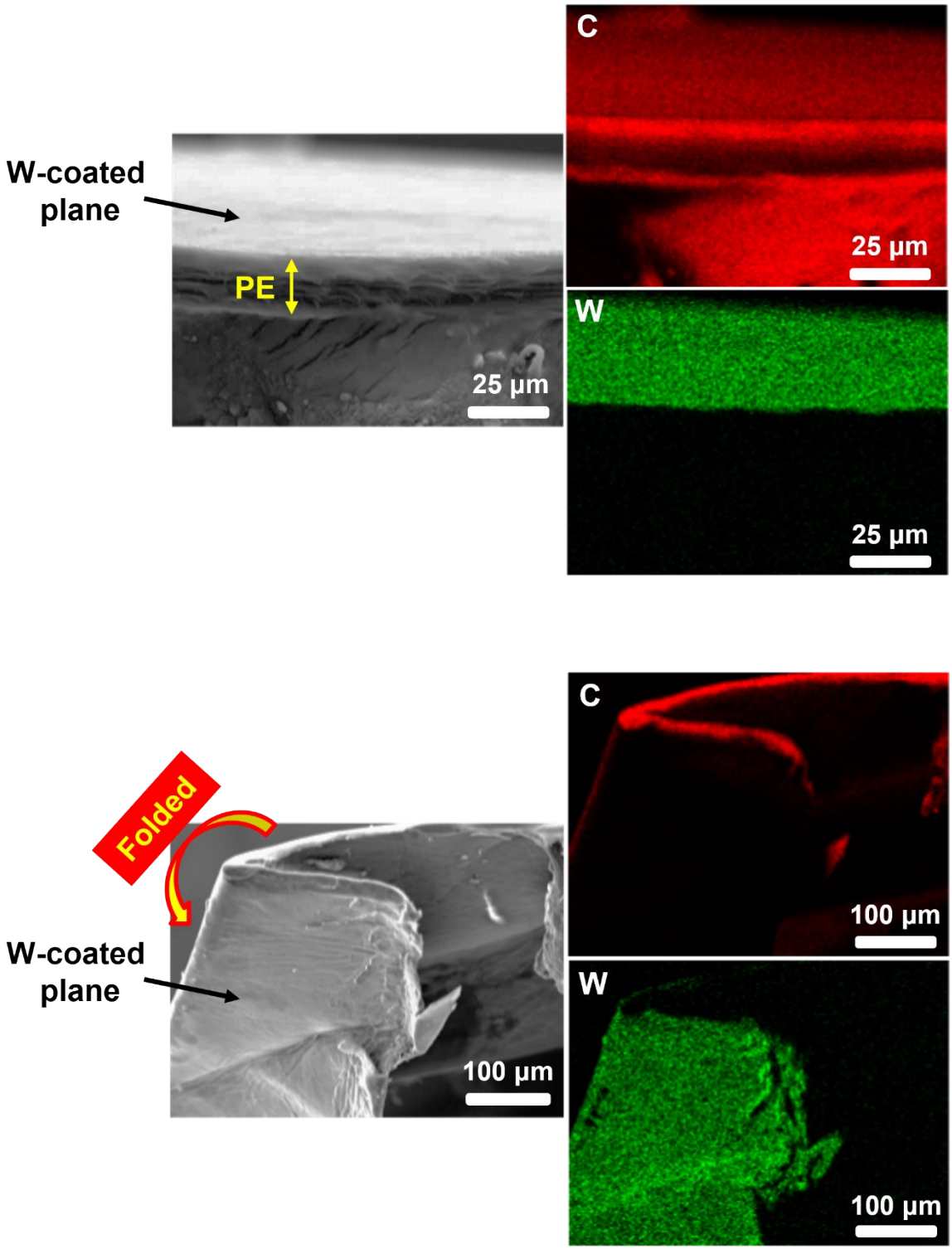

Fig. S3 SEM-EDS images of the W-PE separator.

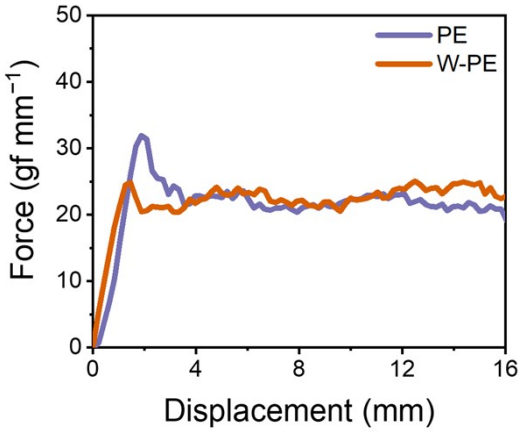

Fig. S4 Peel-off strength measurements of the separators.

Note: Peel-off strength was assessed using a universal testing machine (UTM, QM100s, QMESYS) with 3M Scotch tape applied to separator surfaces and peeled at 10 mm s^{-1}. The comparable peel-off strength between W-PE and bare PE indicates robust W-PE interfacial binding.

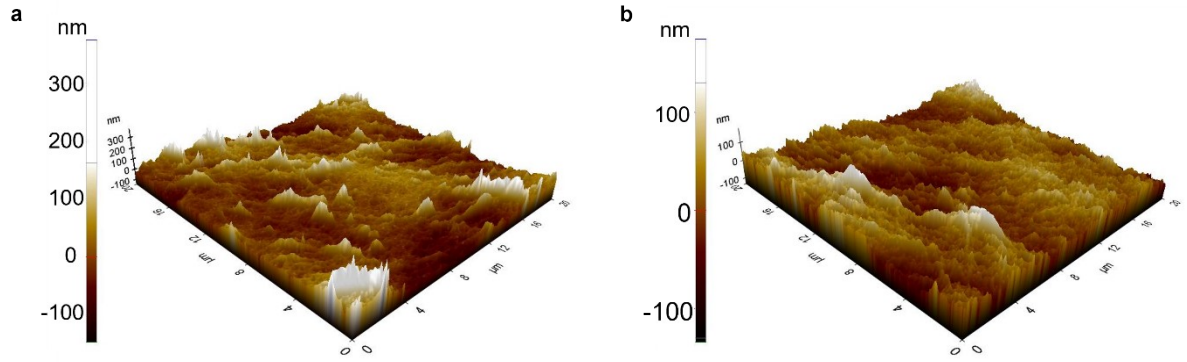

Fig. S5 AFM 3D images of the (a) W-PE and (b) PE separators.

Table. S2 AFM roughness analysis of the W-PE and PE separators.

W-PE	Mean (nm)	0.000
	R_q (nm)	41.258
	R_a (nm)	30.879
PE	Mean (nm)	−0.004
	R_q (nm)	33.174
	R_a (nm)	26.277

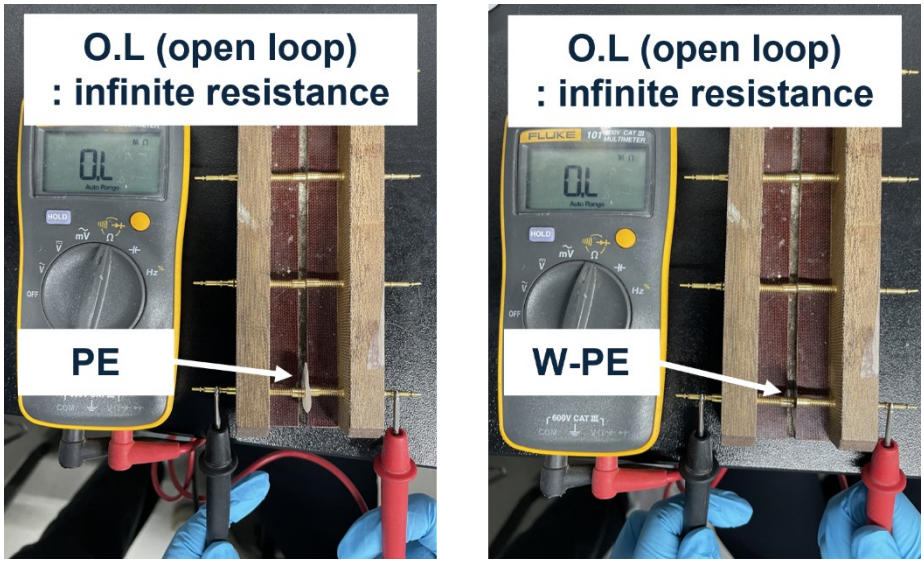

Fig. S6 Electrical conductivities of the PE and W-PE separators. In both cases, an open-loop (O.L.) reading was displayed, indicating negligible electrical conductivity.

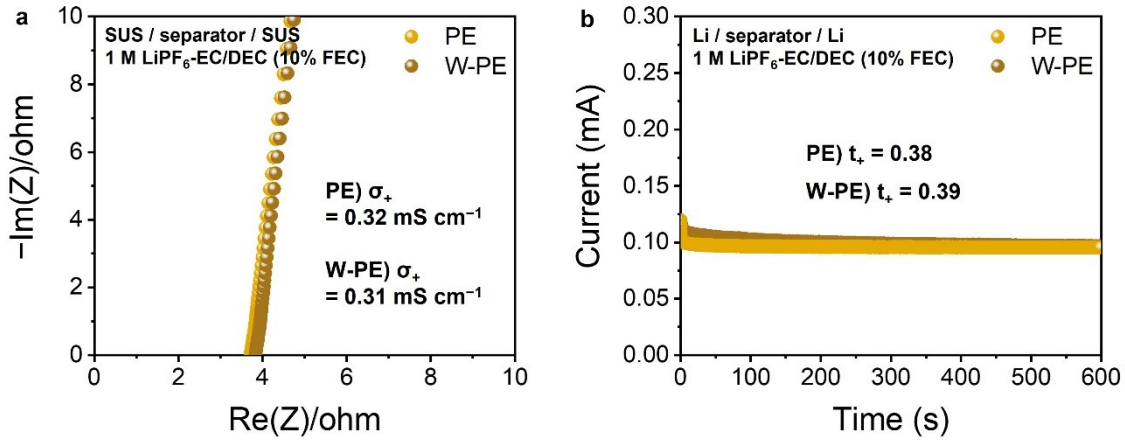

Fig. S7 (a) Ionic conductivity measurement by EIS and (b) Li^+ transference number evaluation using DC polarization technique.

Note: Ionic conductivity and Li^+ transference number were measured using equations below:

$$\sigma = \frac{d}{R_b \times S} \tag{1}$$

$$t_+ = \frac{I_s(\Delta V - I_o R_o)}{I_o(\Delta V - I_s R_s)} \tag{2}$$

(1): d is the thickness of electrolyte-soaked separator, R_b is the bulk resistance, and S is the area of the electrodes.

(2): I_s is the steady-state current, I_o is the initial current, ΔV is the voltage pulse (10 mV), R_o and R_s are the initial and steady-state resistance, respectively.

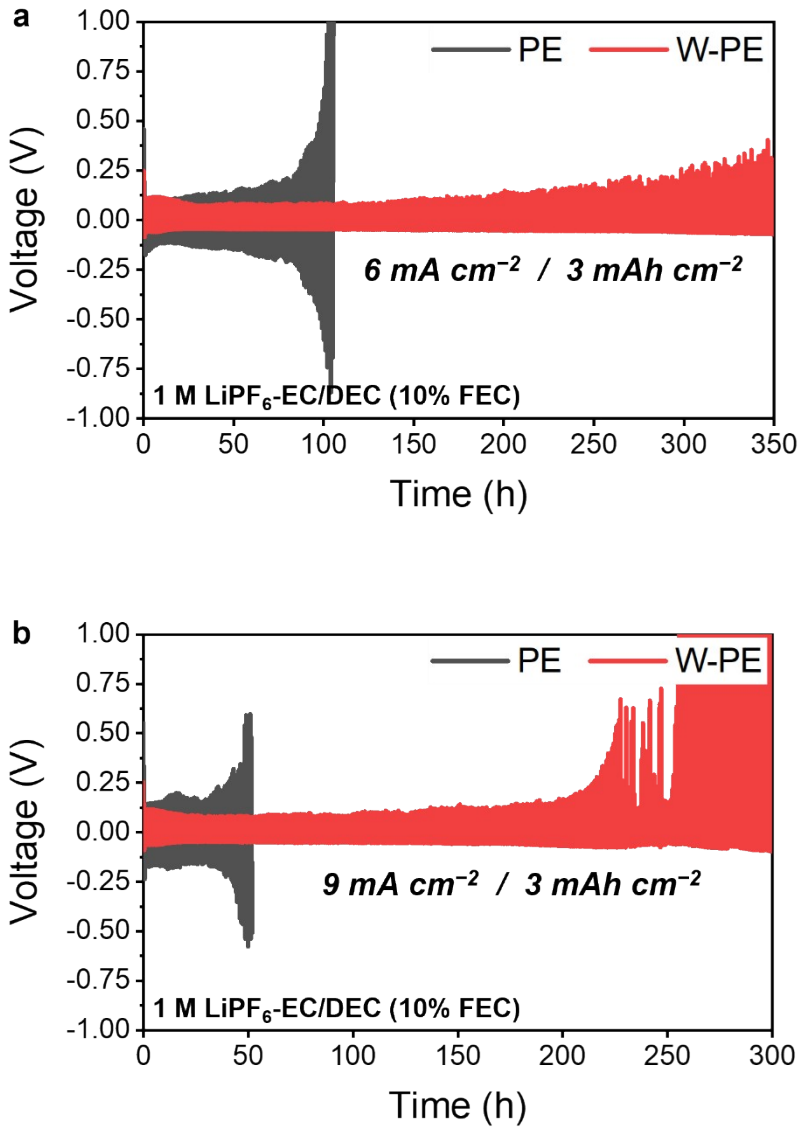

Fig. S8 Evaluation of the Li-Li symmetric cell with the PE and W-PE separators at various current densities and constant capacity of 3 mAh cm^{-2}. Electrolyte: 1 M $LiPF_6$ in EC/DEC (50/50 = v/v) with 10 wt% FEC.

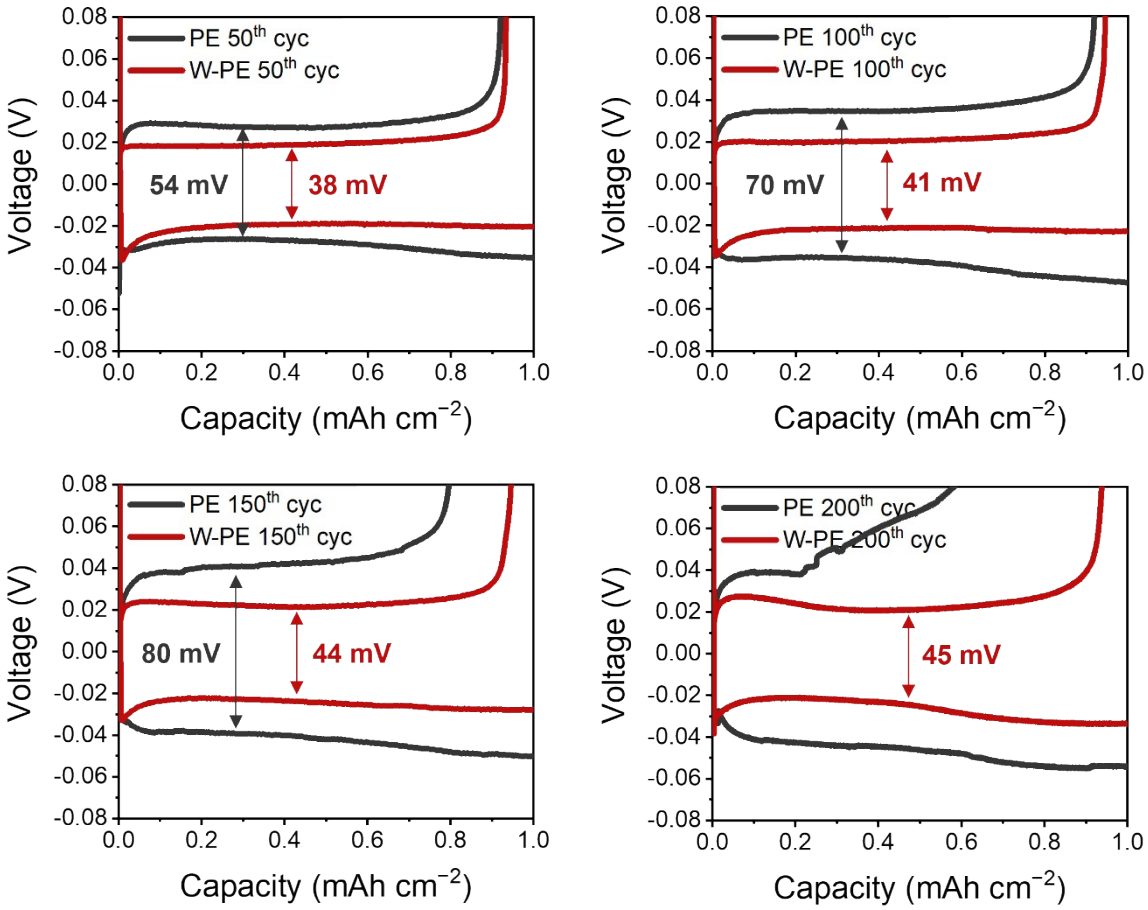

Fig. S9 Voltage profiles of Li-Cu asymmetric cells. Electrolyte: 1 M $LiPF_6$ in EC/DEC (50/50 = v/v) with 10 wt% FEC.

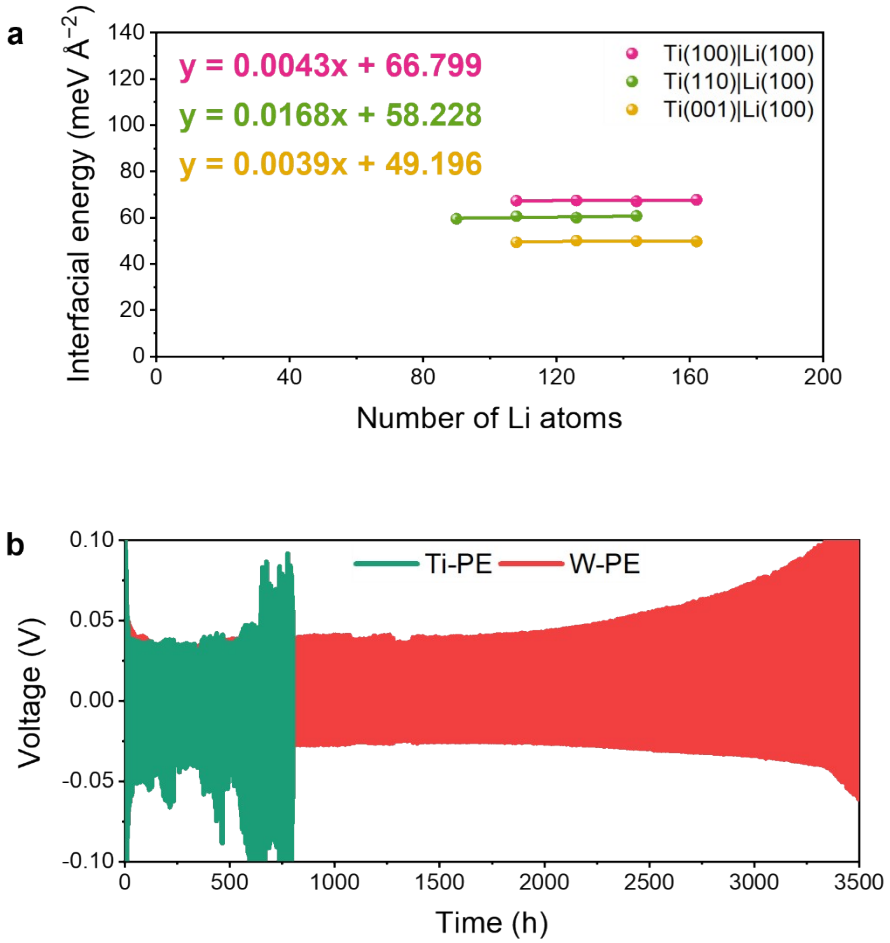

Fig. S10 (a) DFT-calculated Li interfacial energies of Ti metal and (b) voltage profiles of Li-Li symmetric cells with the Ti-PE and W-PE separators, at a current density and capacity of 1 mA cm^{-2} and 1 mAh cm^{-2}, respectively. Electrolyte: 1 M $LiPF_6$ in EC/DEC (50/50 = v/v) with 10 wt% FEC.

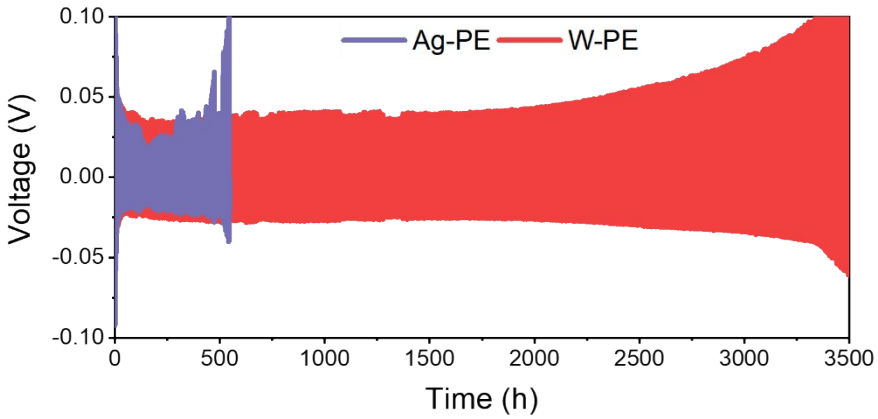

Fig. S11 Voltage profiles of Li-Li symmetric cells with the Ag-PE and W-PE separators, at a current density and capacity of 1 mA cm^{-2} and 1 mAh cm^{-2}, respectively. Electrolyte: 1 M $LiPF_6$ in EC/DEC (50/50 = v/v) with 10 wt% FEC.

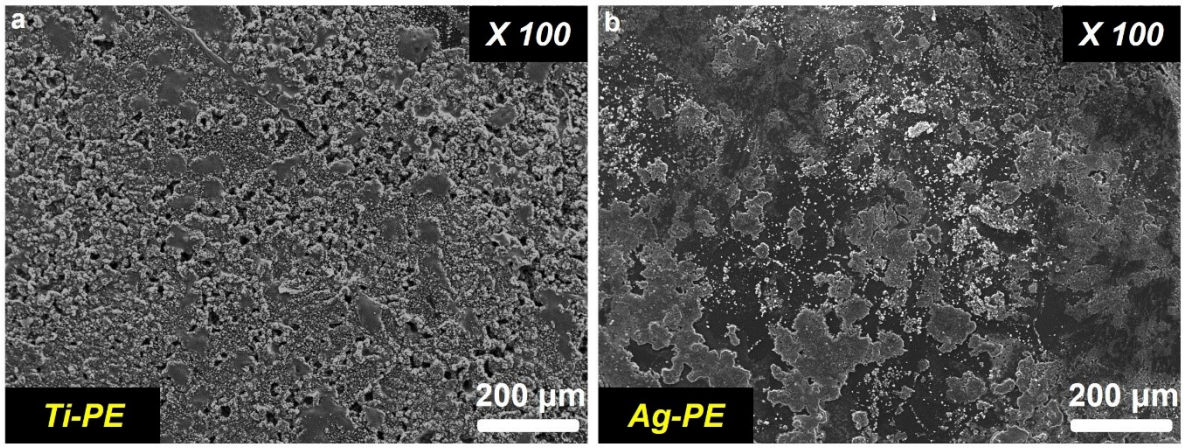

Fig. S12 SEM images of Li metal anodes after the 1st plating at a current density and capacity of 1 mA cm^{-2} and 1 mAh cm^{-2}, respectively, in Li-Li symmetric cells with the (a) Ti-PE and (b) Ag-PE separators.

Table. S3 DFT-calculated Li interfacial energy and Li-Li symmetric cell cycle life for various interface materials.

Interface	Li interfacial E (100)	Li symmetric cell cycle life (1 mA cm^{-2}, 1 mAh cm^{-2})
W	131.1 meV $Å^{-2}$	3500 h
Ti	66.8 meV $Å^{-2}$	800 h
Ag	−10.3 meV $Å^{-2}$	550 h

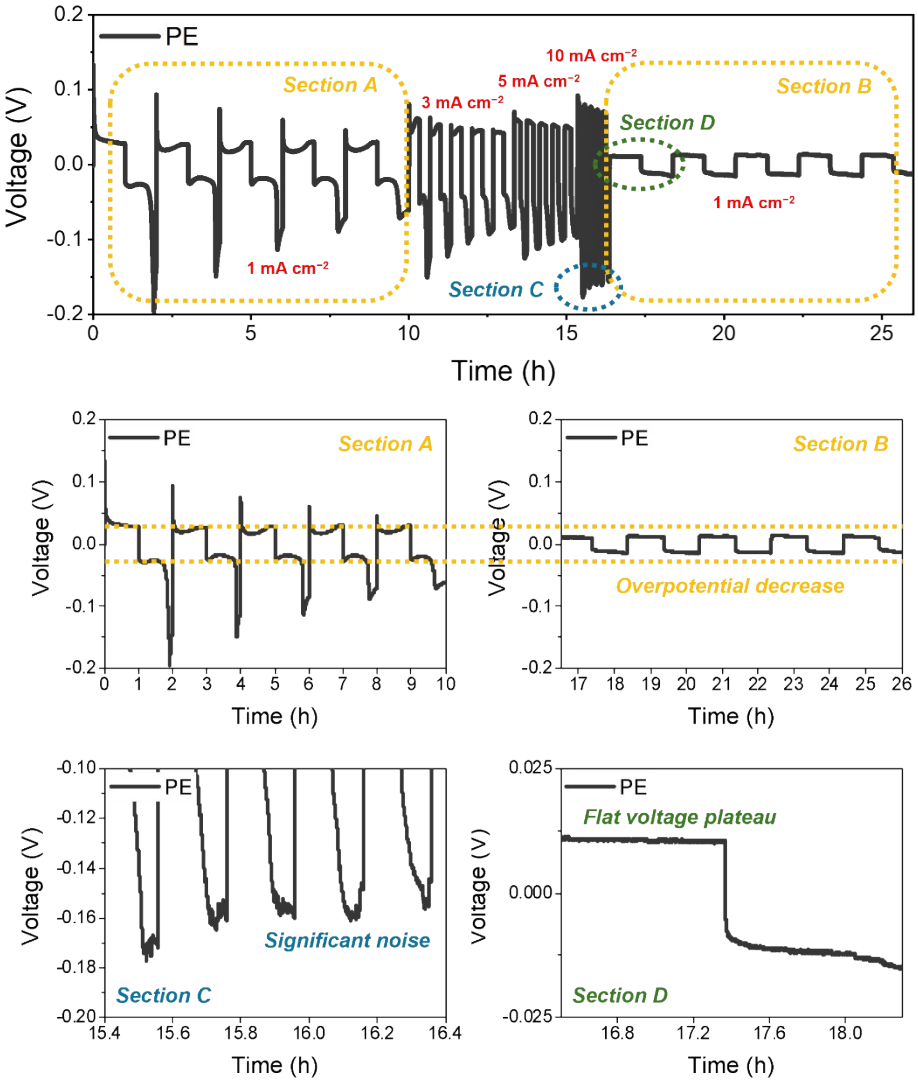

Fig. S13 Evaluation of the Li-Li symmetric cell with the PE separator at various current densities.

Section A, B: 1 mA cm^{-2} / 1 mAh cm^{-2}. The decrease in overpotential when returning to section B after running at high current densities indicates the occurrence of an internal short circuit.

Section C: 10 mA cm^{-2} / 1 mAh cm^{-2}. Significant noise in the voltage profile indicates abnormal current flow.

Section D: After returning to 1 mA cm^{-2}, the voltage profile flattened, characteristic of a soft short circuit, where the overpotential related to Li nucleation and growth remained constant.

Electrolyte: 1 M $LiPF_6$ in EC/DEC (50/50 = v/v) with 10 wt% FEC.

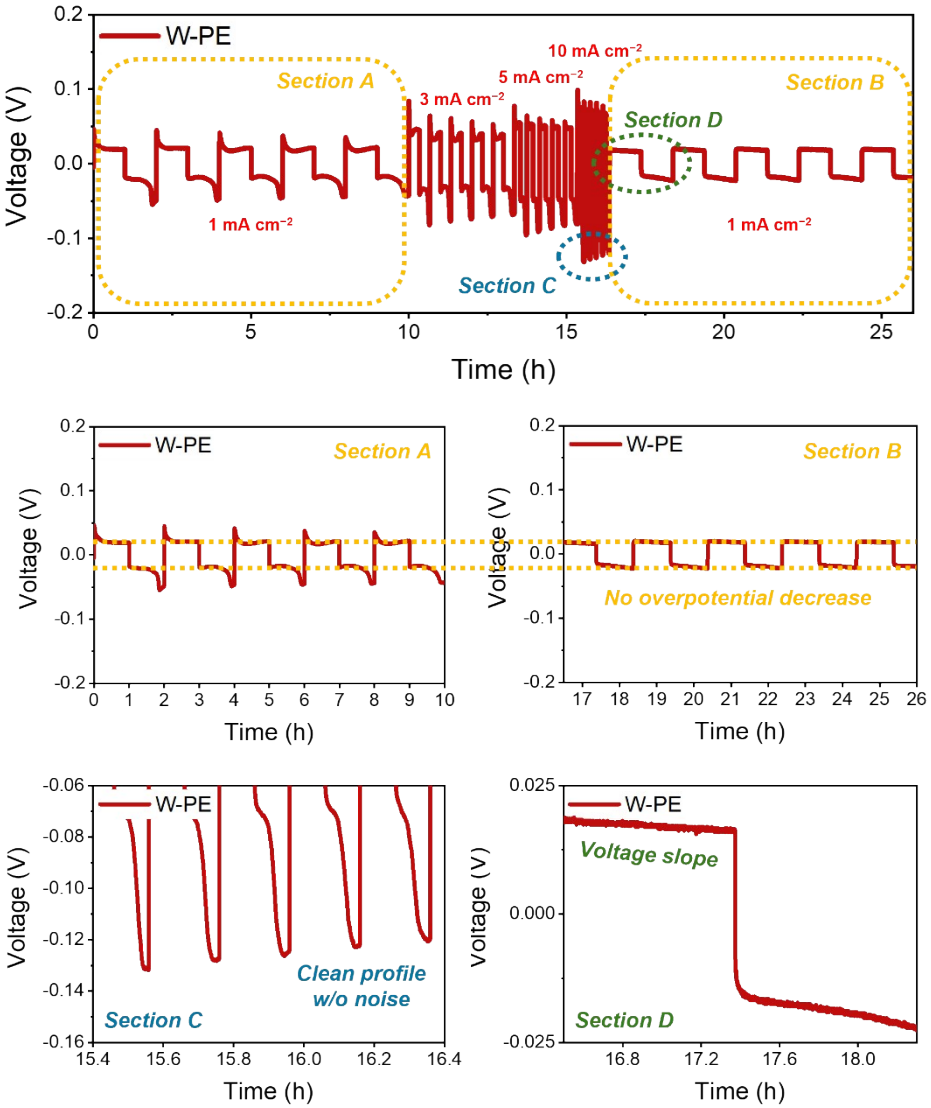

Fig. S14 Evaluation of the Li-Li symmetric cell with the W-PE separator at various current densities.

Section A, B: 1 mA cm^{-2} / 1 mAh cm^{-2}. No decrease in the overpotential when returning to section B after running at high current densities.

Section C: 10 mA cm^{-2} / 1 mAh cm^{-2}. Clean voltage profiles without significant noise.

Section D: After returning to 1 mA cm^{-2}, the voltage profile remained sloped, indicating that the overpotential related to Li nucleation and growth remained different.

Electrolyte: 1 M $LiPF_6$ in EC/DEC (50/50 = v/v) with 10 wt% FEC.

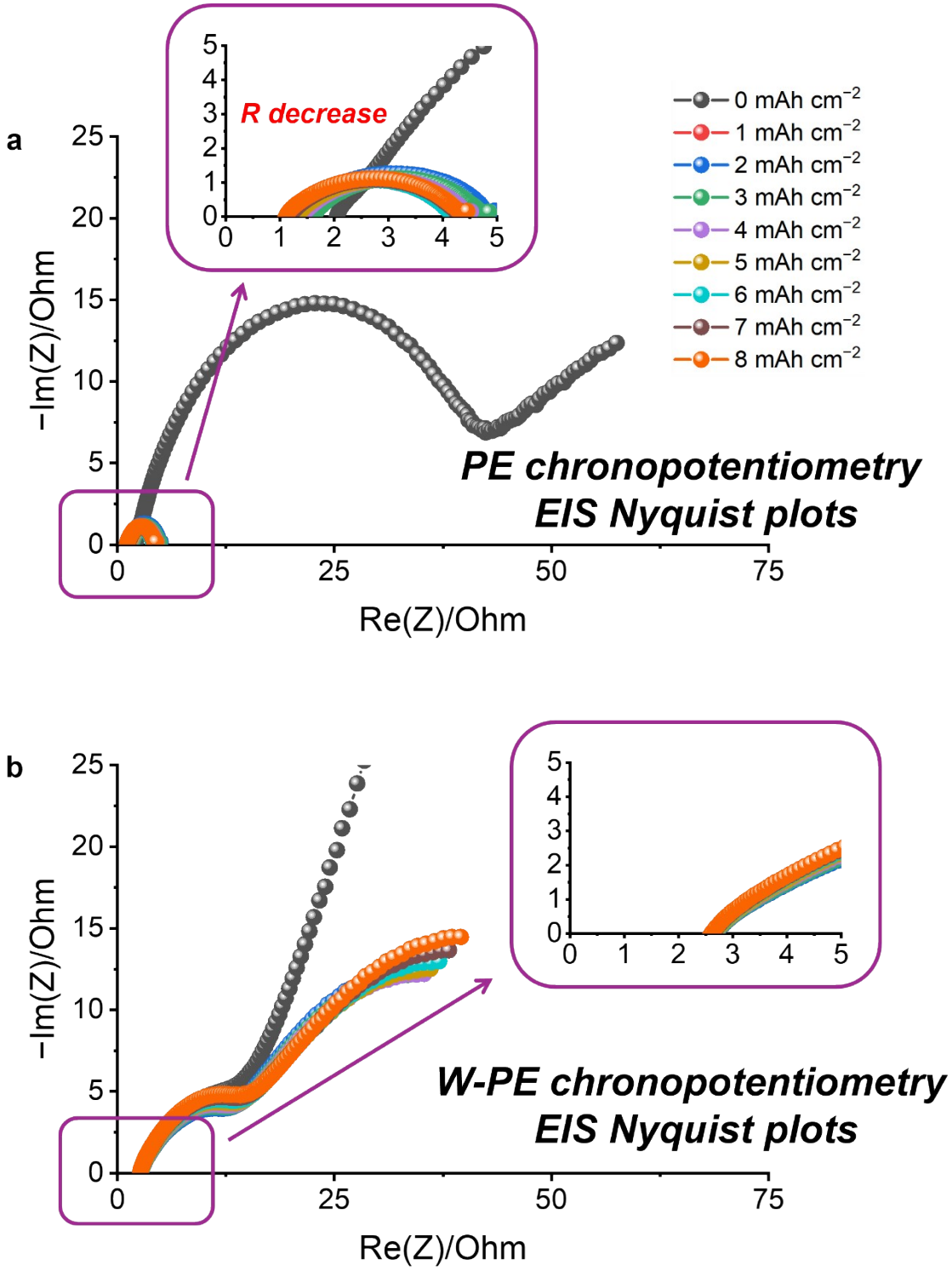

Fig. S15 Nyquist plots from in situ EIS measurements during chronopotentiometry of Li-Li symmetric cells with the PE and W-PE. EIS measurements were recorded hourly (per 1 mAh cm^{-2}) with constant Li plating in a single direction, during which time a current density of 1 mA cm^{-2} was being applied.

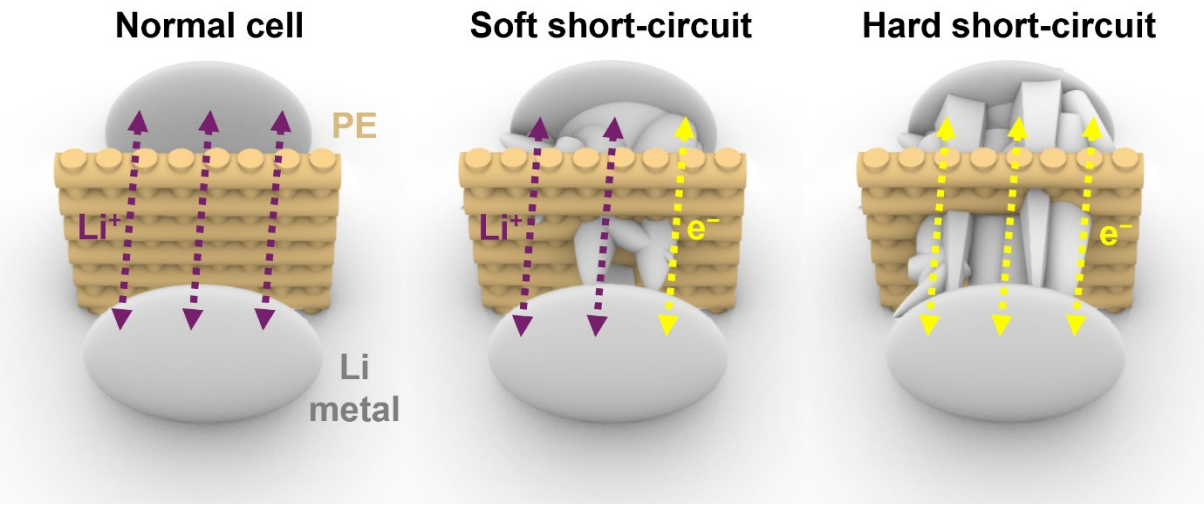

Fig. S16 Schematic illustration of the short-circuit behavior in Li-Li symmetric cells[9]: A soft short circuit is characterized by both significant ionic and electronic conduction through the separator, whereas electronic conduction mainly occurs in hard short circuits resulting from Li dendrite penetration, which establishes direct contact between the two electrodes.

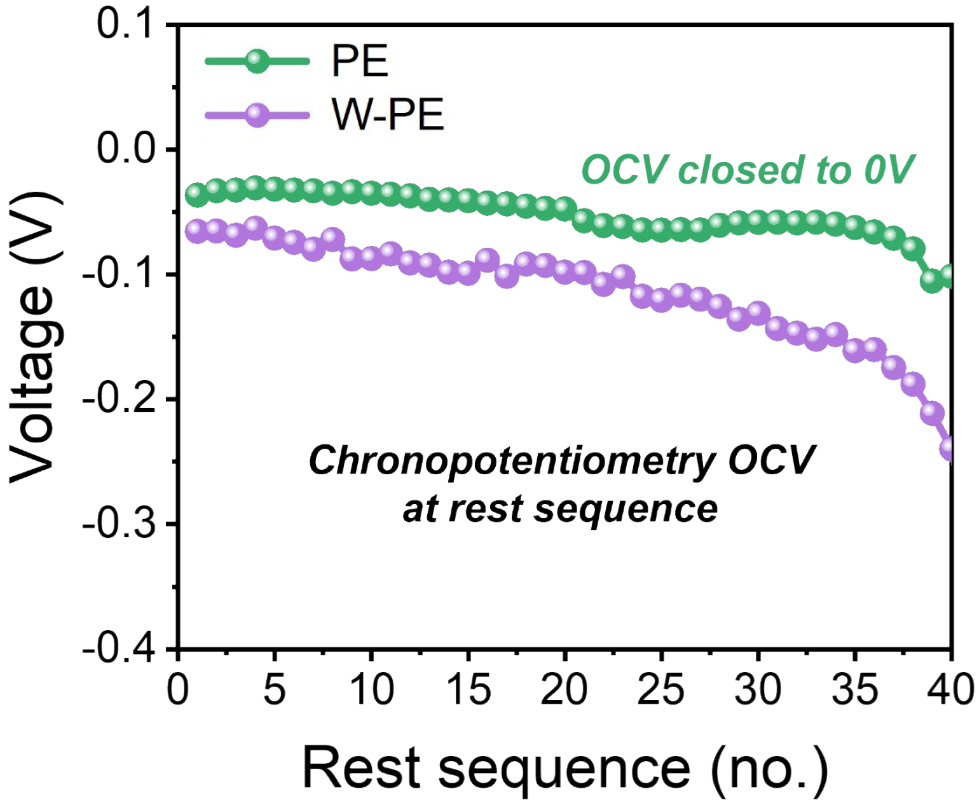

Fig. S17 OCV measurements made in rest sequences during chronopotentiometry of Li-Li symmetric cells. At a current density of 1 mA cm^{-2}, rest periods were taken every hour (per 1 mAh cm^{-2}). OCV close to 0 V for the PE indicates soft short-circuit behavior.

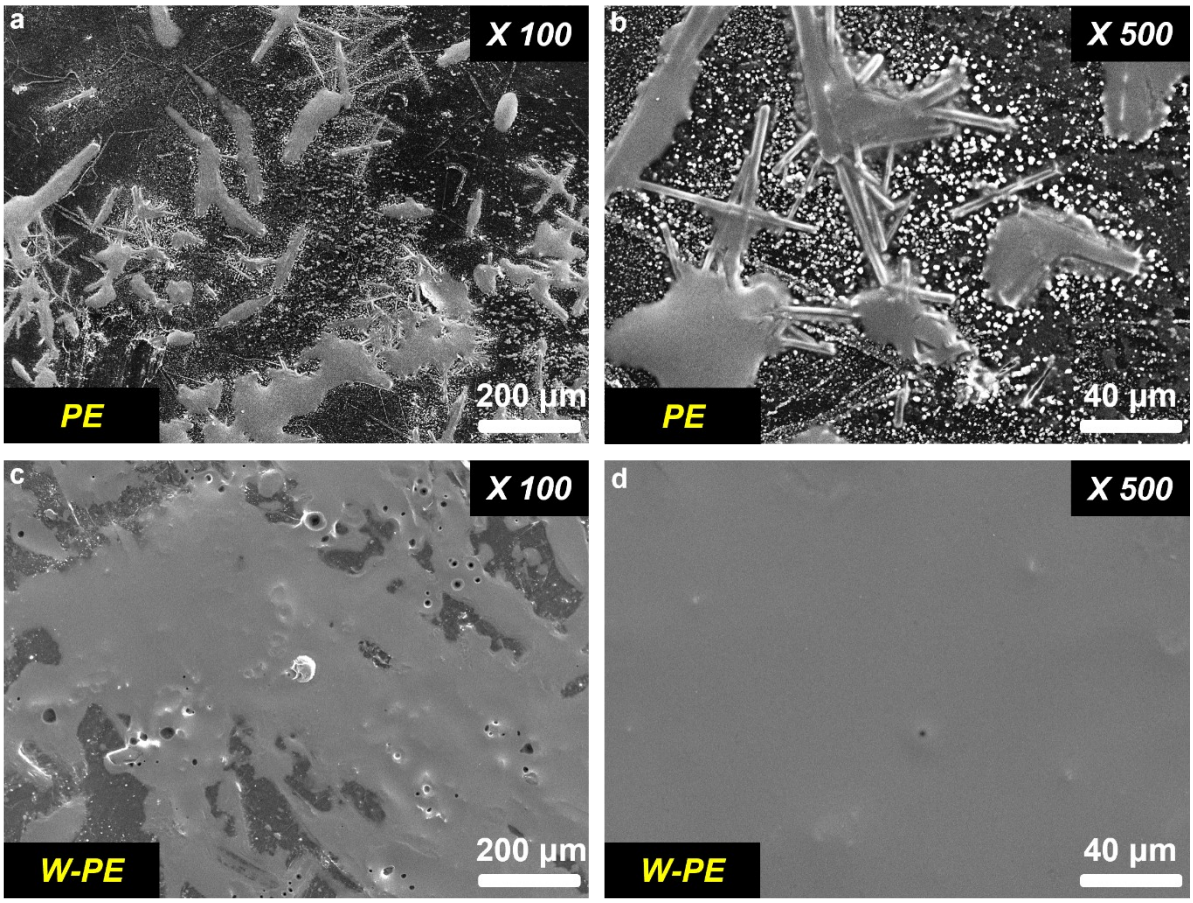

Fig. S18 SEM images of Li metal anodes after the 1st plating at a current density and capacity of 6 mA cm^{-2} and 3 mAh cm^{-2}, respectively, in Li-Li symmetric cells with the respective PE and W-PE separators.

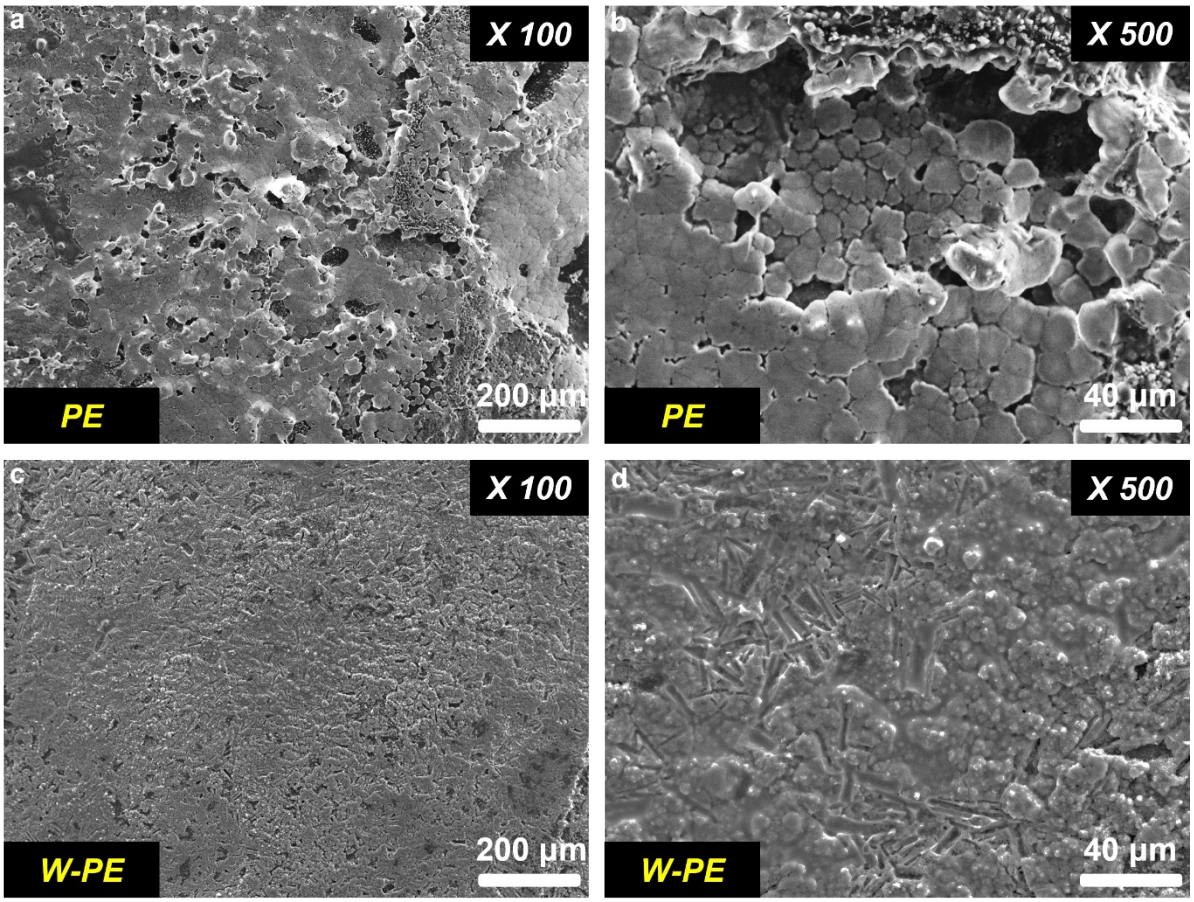

Fig. S19 SEM images of Li metal anodes after the 1st stripping at a current density and capacity of 3 mA cm^{-2} and 3 mAh cm^{-2}, respectively, in Li-Li symmetric cells with the respective PE and W-PE separators.

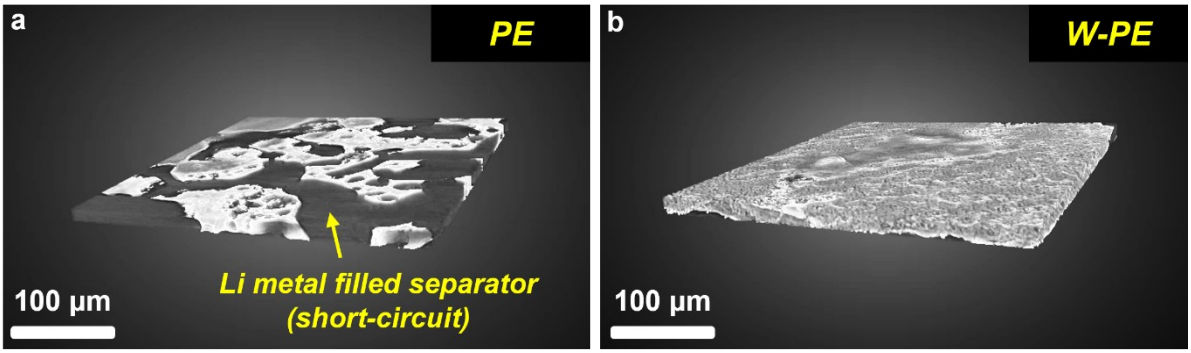

Fig. S20 XRM 3D images of the PE and W-PE separators in Li-Li symmetric cells after 100 cycles.

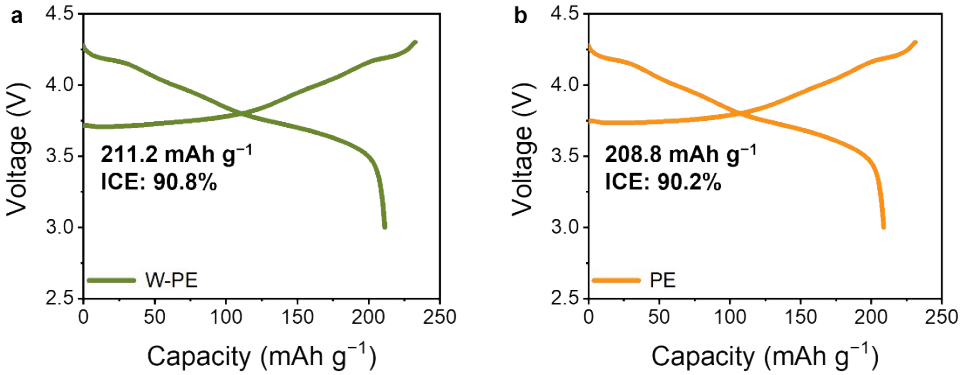

Fig. S21 Full-cell 1st cycle voltage profiles with the (a) W-PE and (b) PE separators at a current density of 0.1C (1C = 3.0 mA cm^{-2}). Electrolyte: 1 M $LiPF_6$ in EC/DEC (50/50 = v/v) with 10 wt% FEC.

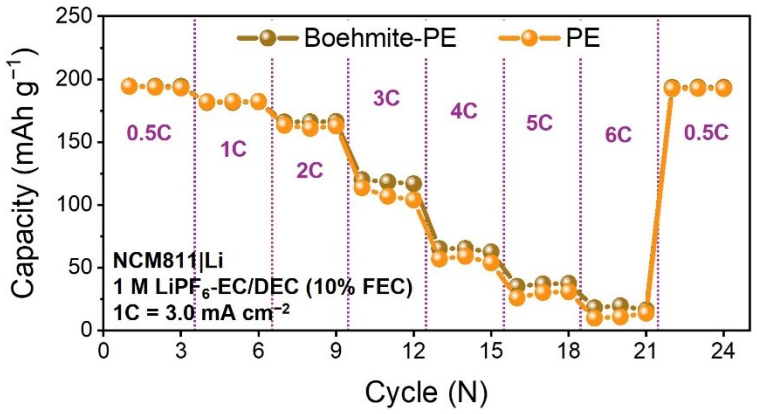

Fig. S22 Rate capability test results of full-cells with and without boehmite coating on PE (1C = 3.0 mA cm^{-2}) when a conventional carbonate-based electrolyte (1 M $LiPF_6$ in EC/DEC with 10% FEC) was used.

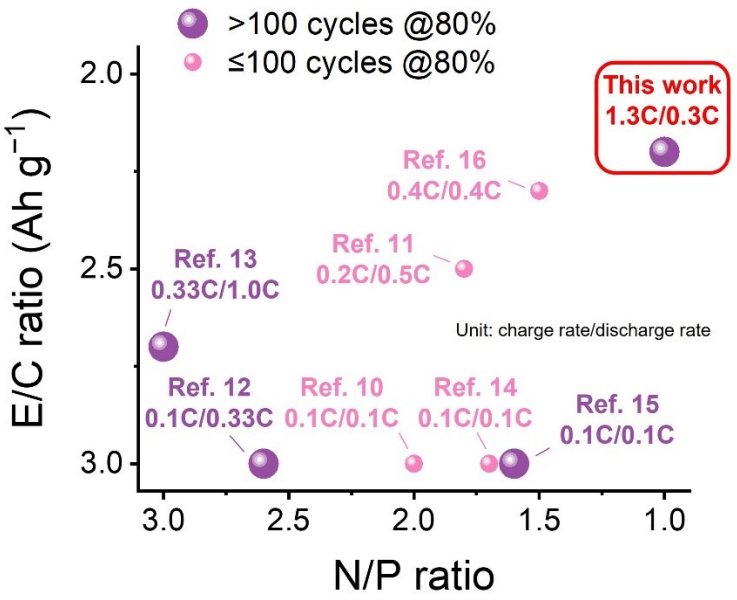

Fig. S23 Performance comparison of LMB studies under constrained Li metal and electrolyte resources (N/P ratio < 3 and E/C ratio < 3).[10-16]

References

1. G. Kresse and J. Furthmüller, *Comput. Mater. Sci.*, 1996, **6**, 15-50.
2. J. P. Perdew, K. Burke and M. Ernzerhof, *Phys. Rev. Lett.*, 1996, **77**, 3865-3868.
3. A. van de Walle and G. Ceder, *J. Phase Equilib.*, 2002, **23**, 348.
4. A. van de Walle, M. Asta and G. Ceder, *Calphad*, 2002, **26**, 539-553.
5. Y. Zhao, T. Zhou, M. Mensi, J. W. Choi and A. Coskun, *Nat. Commun.*, 2023, **14**, 299.
6. J. Oh, S. H. Choi, H. Kim, J. Y. Kim, G.-J. Lee, K. Y. Bae, T. Lee, N. Lee, Y. Sohn, W. J. Chung and J. W. Choi, *Energy Environ. Sci.*, 2024, **17**, 7932-7943.
7. N. D. Lepley and N. A. W. Holzwarth, *Phys. Rev. B*, 2015, **92**, 214201.
8. J. Sangster and A. D. Pelton, *J. Phase Equilib.*, 1991, **12**, 203-203.
9. Q. Li, A. Chen, D. Wang, Z. Pei and C. Zhi, *Joule*, 2022, **6**, 273-279.
10. W. Deng, W. Dai, X. Zhou, Q. Han, W. Fang, N. Dong, B. He and Z. Liu, *ACS Energy Lett.*, 2021, **6**, 115-123.
11. P. Zhao, Y. Li, S. Chen, H. Fan, Y. Feng, L. Hu, Y. Zhang, Q. Nie, H. Pei, C. Yang, J. Deng, C. Bao and J. Song, *Adv. Energy Mater.*, 2022, **12**, 2200568.
12. C. Niu, H. Lee, S. Chen, Q. Li, J. Du, W. Xu, J.-G. Zhang, M. S. Whittingham, J. Xiao and J. Liu, *Nat. Energy*, 2019, **4**, 551-559.
13. Y. Gao, M. Guo, K. Yuan, C. Shen, Z. Ren, K. Zhang, H. Zhao, F. Qiao, J. Gu, Y. Qi, K. Xie and B. Wei, *Adv. Energy Mater.*, 2020, **10**, 1903362.
14. P. Shi, X.-Q. Zhang, X. Shen, B.-Q. Li, R. Zhang, L.-P. Hou and Q. Zhang, *Adv. Funct. Mater.*, 2021, **31**, 2004189.
15. C. Niu, H. Pan, W. Xu, J. Xiao, J.-G. Zhang, L. Luo, C. Wang, D. Mei, J. Meng, X. Wang, Z. Liu, L. Mai and J. Liu, *Nat. Nanotechnol.*, 2019, **14**, 594-601.
16. X.-Q. Zhang, T. Li, B.-Q. Li, R. Zhang, P. Shi, C. Yan, J.-Q. Huang and Q. Zhang, *Angew. Chem., Int. Ed.*, 2020, **59**, 3252-3257.